



**HAL**  
open science

## Stress-driven method bio-inspired by long bone structure for mechanical part mass reduction by removing geometry at macro and cell-unit scales

Mathieu Bilhère-Dieuzeide, Julien Chaves-Jacob, Emmanuel Buhon,  
Guillaume Biguet-Mermet, Jean-Marc Linares

### ► To cite this version:

Mathieu Bilhère-Dieuzeide, Julien Chaves-Jacob, Emmanuel Buhon, Guillaume Biguet-Mermet, Jean-Marc Linares. Stress-driven method bio-inspired by long bone structure for mechanical part mass reduction by removing geometry at macro and cell-unit scales. *Materials & Design*, 2022. hal-03582896

**HAL Id: hal-03582896**

**<https://hal.science/hal-03582896>**

Submitted on 21 Feb 2022

**HAL** is a multi-disciplinary open access archive for the deposit and dissemination of scientific research documents, whether they are published or not. The documents may come from teaching and research institutions in France or abroad, or from public or private research centers.

L'archive ouverte pluridisciplinaire **HAL**, est destinée au dépôt et à la diffusion de documents scientifiques de niveau recherche, publiés ou non, émanant des établissements d'enseignement et de recherche français ou étrangers, des laboratoires publics ou privés.

## Title:

Stress-driven method bio-inspired by long bone structure for mechanical part mass reduction by removing geometry at macro and cell-unit scales

## 5 Authors:

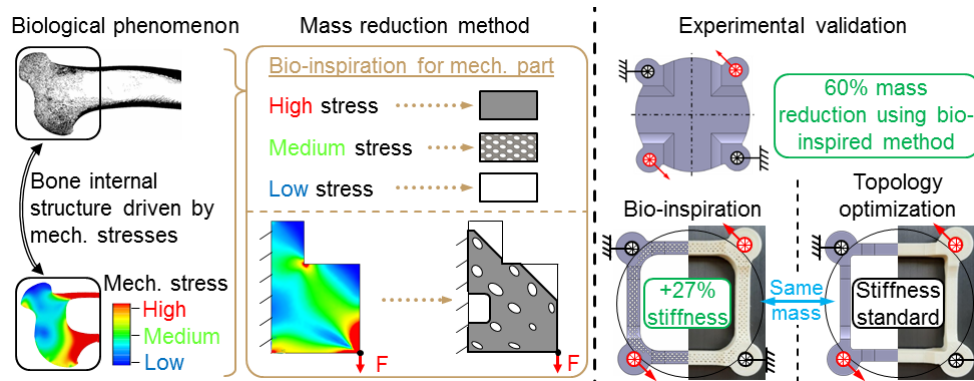
Mathieu Bihère-Dieuzeide<sup>a, b</sup>, Julien Chaves-Jacob<sup>a, \*</sup>, Emmanuel Buhon<sup>b</sup>, Guillaume Biguet-Mermet<sup>b</sup>, Jean-Marc Linares<sup>a</sup>

<sup>a</sup> Aix-Marseille Univ, CNRS, ISM, Inst Mouvement Sci, UMR 7287, Marseille, France

<sup>b</sup> Thales LAS (Land Air System) France OME (Optronics and Missile Electronics), Elancourt, France

10 \* Corresponding author: [julien.chaves-jacob@univ-amu.fr](mailto:julien.chaves-jacob@univ-amu.fr) (J. Chaves-Jacob)

## Graphical abstract:



## Highlights:

- 15
- Proposed mass reduction method is bio-inspired from long bones, from both medullar cavity and trabecular bone structures
  - Experimental testing was carried out to compare the mechanical performances offered by the method with topology optimization at equal mass
  - Presented 2.5D torsion disc mass was reduced by 60% compared to the initial disc
- 20
- Bio-inspired design of the sample is 27% stiffer, at equal mass, than the one obtained through topology optimization

## Abstract:

25 Mass reduction is a main issue in mechanical design. Over millions of years, Nature had to face this issue. Nature came up with an efficient solution using a stress-driven structure to reduce the mass of bones while saving their mechanical performances. This optimized structure is used in several species and persists throughout Evolution. Thus, it may be considered as optimal for this issue. In this article, a method bio-inspired from both bone medullar cavity and trabecular structure is proposed to reduce the mass of parts subjected to mechanical stresses. The objective of this method is to provide high mass reduction, just like bone does. First, the method removes iteratively unloaded areas of material from the mechanical part to mimic the medullar cavity structure. Second, a final mass reduction is done integrating small holes bio-inspired from trabecular structure in the remaining material. An experimental validation was carried out on a torsion disc and provided a 60% mass reduction. Using this mass reduction rate, the topology optimization method was used to define a standard geometry to evaluate the mechanical performances of the proposed

30

35 method. Experimental results highlight that regarding torsional stiffness, the bio-inspired part is 27% stiffer than the standard one.

Keywords:

Bio-inspiration ; Bio-mimicry ; Bone structure ; Mass reduction ; Stress-driven ; Topology optimization

# 1 Introduction

Mechanical part mass reduction is a major issue in design and numerous methods have been developed to deal with this subject. In the last years, a rise of these methods was allowed by the spread of metallic additive manufacturing [1]. Indeed, with additive manufacturing, the production costs and the part complexity become uncorrelated. This property allows for parts with complex internal structures to be manufactured. These geometric possibilities can be integrated in design methods that have a mass reduction objective.

The most known and used mass reduction method is the topology optimization (TO). Indeed, it is an industrially proven method developed during the 80s [2]. It has been implemented and upgraded by CAD software editors. In general, this method is used to satisfy a mass reduction goal while maximizing the mechanical part stiffness under a mechanical loading. In this method, the obtained geometry is largely influenced by the initial part design, especially in 2D simulations [3], and by the mechanical loadings [4]. In TO, if the loading localization is different from the nominal one used to initiate the optimization process, a drastic decrease of mechanical performances of the part is observed [5]. Furthermore, the macro-scale topology proposed in this method is based on the design of large hollow or solid material areas organized as slender beams on the studied mechanical part [6] [7].

To address the TO behavior, a new type of structure emerged: the uniform lattice structures [8]. These structures are composed of cell unit repetitions. At the cell unit scale, the method also proposes hollow or solid material areas organized as slender beams. But at the macroscale, the volume fraction concept is provided in these uniform lattice structures. At this scale, instead of being located as in TO, the void is homogeneously spread over the studied part. This property can influence wide domains such as osteointegration in graft engineering [9] and mechanical engineering. In uniform lattice structures, two types of model structures were developed: the first ones are the strut-based structures and the second ones are the Triply Periodic Minimal Surface structures (TPMS). Both structures allow for a better void distribution at the macroscale. Moreover, the unit cell parameters such as their size or their thickness have a great influence on the part's mechanical performances [10] [11]: smaller porosities provide higher mechanical performances. Strut-based structures are composed of a beam network arrangement [12]. Many studies have shown the effectiveness of these structures that allow numerous options of design [13] [14]. In particular, medical engineering works have demonstrated the influence of the beam orientations [15]. On the other hand, the strut-based structures are only composed of sharply jointed beams. These joints generate local tangential discontinuities that give rise to stress concentrations [16], which can contribute to local cracks. These tangential discontinuities have been reduced by the use of TPMS that present smoother shapes to limit stress concentrations [17] [18] [19].

However, uniform lattice structures are homogeneous structures that can involve a limit in mass reduction optimization. In these methods, the highest mechanical stress value is used to define a unique oversized volume fraction. In consequence, it limits the mass reduction. To go further in mass reduction optimization, gradient lattice structures are proposed. Gradients structures are mechanical stress-driven methods. The local volume fraction is adapted by varying the unit cell thickness according to mechanical stress [14]. High stress areas have a high volume fraction and low stress areas have low volume fraction [20]. With this variation, it is possible to reach an optimized mechanical strength-to-weight ratio. This gradient approach can be used with the strut -based structures [21] [22] [20] or with the TPMS geometry [13] [23].

To satisfy mass reduction objectives, bio-inspired methods were developed. Nature becomes a great source of inspiration in terms of optimization and structure adaptation. Bio-inspiration can take many forms in a mass reduction process. Internal bone structure was observed by *Ghazlan et al.* [24]. In this work, the internal trabecular bone structure was mimicked, in order to design a hybrid concave/convex cell organized in thin-wall structure. The authors compared this hybrid structure with traditional thin-wall structures such as honeycomb or hexagonal re-entrant structures. They showed the effectiveness in compressive stiffness of their structure. In another work, a structure built out of unit cells made of beams was mimicked from the hexactinellid sponge [25]. In this study, the proportion between the cell size and the thickness of the beams has been inspired by the one observed in the sea sponge. Bio-inspiration can also be combined with optimization process [26]. The method bio-inspired by the fish bone presented by Wang et al. [27] is an

example of these mixed processes. This method mixed observations of fish bone, use of load path optimization process and use of size optimization process. Fillet radii were added to reduce tangential discontinuities and thus stress concentrations. They showed the effectiveness in structural stiffness of their structure. Nevertheless, as in uniform lattice methods, the cell unit size (or the pattern size) was selected manually by the user [22]. In most bio-inspired methods, iterations were needed to determine the appropriate pattern size for a given application. A fully bio-inspired mass reduction process was developed by Audibert et al. [5]. A mass reduction method was defined in this work. This method was applied on a plane and thereafter the resulting geometry was extruded along the orthogonal direction. In the rest of this paper, this type of geometries is referred as “2.5D” geometries. In the method, the parameters of patterns (shape and size) and porosities (size and orientation) were bio-inspired by trabecular bone structure. The authors showed the effectiveness of their method compare to TO method in terms of mass reduction and structural stiffness. This method shows a lower limit in terms of material volume fraction that is about 55% (thus the maximum mass reduction is about 45%).

In this paper, a new iterative bio-inspired method based on the bone ontogenesis and remodeling is proposed to improve the mass reduction in 2.5D. This method will be called “Bio-Inspired Mass Reduction Iterative Method” (BIMRIM). A first section will present the biological principles used in the method, more specifically the long bone structure and the medullar cavity development mechanism (Section 2). A second section will present the iterative mass reduction process (Section 3). In a third section, the evaluation of the effectiveness of this method will be shown (Section 4). The TO method was set as the standard for comparing methods. Two parts with the same mass were 3D-printed. An experimental test was carried out on a torsion disc. The torsional stiffness of both parts was compared.

## 2 Nature database for mass reduction: osteogenesis and bone remodeling principles mimicry

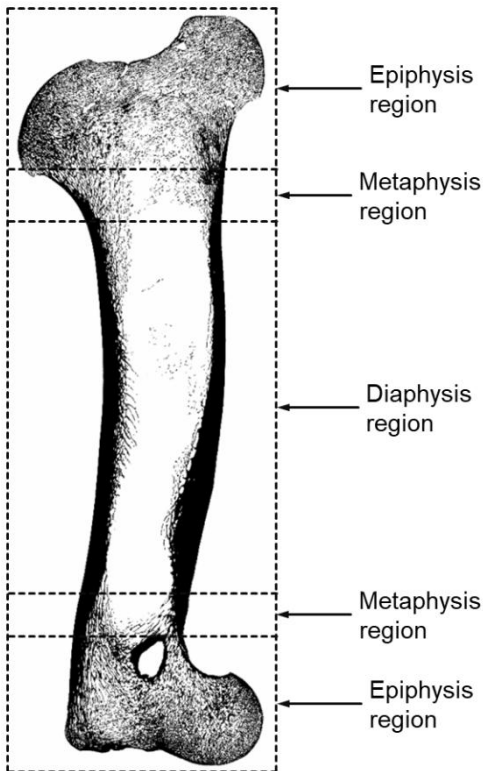
The design of light and stiff mechanical part is an issue that Nature has been facing since millions of years. Numerous stiff and light solutions are present in the database of Nature [28] [29]. Among these solutions, endoskeletons are widely spread in Nature, especially in animals. Endoskeletons are composed of bones with complex internal structure. Whether it is the internal structure of bones or designed structures seen in Section 1, they are both too complex to be manufactured through conventional manufacturing. Additive manufacturing offers new possibilities for producing this kind of structures. These manufacturing processes allow to consider the design of complex structures mimicking the bone internal structure.

The method developed thereafter uses additive manufacturing possibilities while being bio-inspired by endoskeleton bones, and more precisely by long bone structure. Indeed, the objectives of the method are to reduce the mass of mechanical part while maintaining high mechanical performances, objectives fulfilled by bones. Moreover, bone is the outcome of millions of years of evolution that led to this structure in several species. In addition, as for most structures of Nature, bones use the minimum amount of energy and resources (food, water, ...) to get the best properties possible. For these reasons, this structure is considered as optimized for the objectives it satisfies: being light and stiff.

The skeleton is composed of three types of bones: long bones, short bones and plate-like bones. Long bones are made to resist bending and buckling as defined in [30]. Exposure to these mechanical loadings is common in mechanical part under loading. For that reason, BIMRIM is bio-inspired from long bones.

For a human or animal adult, a long bone is composed of three main regions. The diaphysis region is the central part of the bone, followed by the metaphysis region, which makes the transition to the epiphysis region at the bone’s ends (Fig. 1). The diaphysis region is composed of cortical bone that consists in a fully dense compact bone material that surrounds the medullar cavity [31]. The epiphysis is made of trabecular bone, which can be described as a combination of thin wall bone material called trabecula, and void called porosities [31].

140 Bone structure underwent a natural optimization process since bone material is used only in mechanically loaded areas [32].



145 **Fig. 1.** Mid-section tomography of a horse humerus on which three parts can be identified: (1) the diaphysis region, (2) the metaphysis region, and (3) the epiphysis region. This tomography has been obtained through a partnership between FUNEVOLMECADEV MNHN team and CBI ISM AMU team

### 2.1 Wolff's law

150 The main concept used in bone bio-inspired method is the Wolff's law. It describes the ability of the bone structure to adapt its internal structure to the loadings it undergoes during its life [33] [34]. In trabecular bone, the local loadings generate specific local internal bone structure with specific bone material parameters [35]. The thickness of the local bone material (hence of the trabecula) is determined by the local stress field. Commonly, the trabecular orientation is defined by the orientation of local mechanical principal stresses. High mechanical stresses lead to thick trabecula and dense material [36] [37]. Similarly, low mechanical stresses lead to thin trabecula and porous material.

### 2.2 Medullar cavity appearance

155 The bone structure evolves during its whole life, mainly due to the subject's movements and locomotion habits. Locomotion is the major factor in the osteogenesis as explained in [38]. Local mechanical loadings on the long bones are generated by this motion. In turn, these loadings generate mechanical stresses in bone material. Bone-turnover mechanism adapts the bone structure to the loadings. **Indeed, bone has a biological feedback system, involving specific cells, that regulates its local microarchitecture, thus its structure [31]. This bone-turnover, that is an iterative and multi-physical process [39], is composed of growth, modeling, and remodeling of the bone. For human beings, this turnover takes place at least every four months [40] (every four months for cortical bone and six months and a half for the trabecular bone [9]). In the remodeling step [31], the osteocytes iteratively receive the signal generated from mechanical loading changes and trigger the osteoblasts and the osteocytes to form and resorb bone material [39].** Bone material is created to face higher mechanical stresses (formation mechanism). Concurrently, the resorption mechanism removes bone material if the mechanical stresses decrease or if the bone material is too aged [41].

170 The medullar cavity appearance process is widely spread on long bones of many species. Fig. 2 illustrates this mechanism for human beings. Bone development process starts in the early embryo life of the fetus. During the first year (Fig. 2a), the baby locomotion is limited and generates random mechanical loading on

the long bones involved in locomotion. The bone diaphysis region can be described as a homogeneous porous non-oriented bone. At this age, the diaphysis is holed in its center. It is the beginning of the medullar cavity growth. The epiphysis regions are made of cartilage material. After the first year of life, the bipedal posture becomes the main way of locomotion for humans (Fig. 2b). This new locomotion mode orients the mechanical loadings in the bones. As a result, it orients the bone material structure [38]. With this motion change, the diaphysis region undergoes two main modifications: the medullar cavity grows and the remaining bone becomes cortical bone. The epiphysis region composed of cartilage is also transformed into trabecular bone.

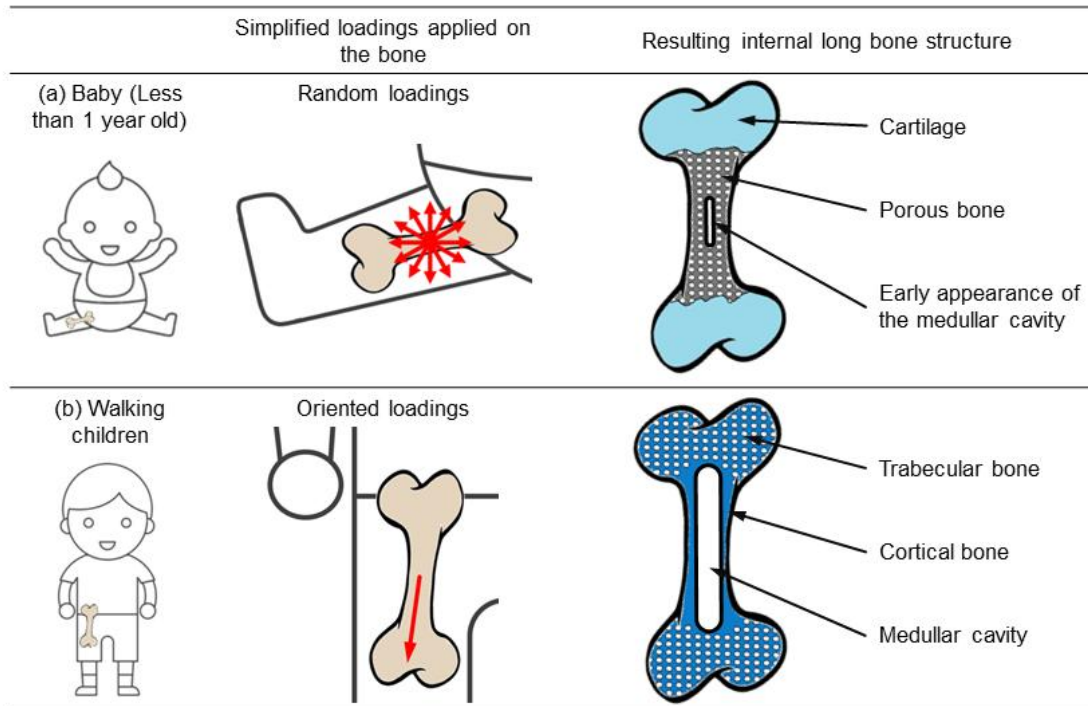


Fig. 2. Evolution of the bone structure depending on the locomotion of the individual

### 3 Bio-Inspired Mass Reduction Iterative Method (BIMRIM)

The proposed mass reduction method is bio-inspired by long bones from endoskeletons of terrestrial mammals. In the first stage, the mass reduction method, bio-inspired by trabecular bone structure, is investigated. In the second stage, the medullar cavity is studied and integrated to BIMRIM in order to improve mass reduction.

#### 3.1 Determination of material cohesion domain

This subsection investigates the material cohesion threshold of Audibert's method [5].

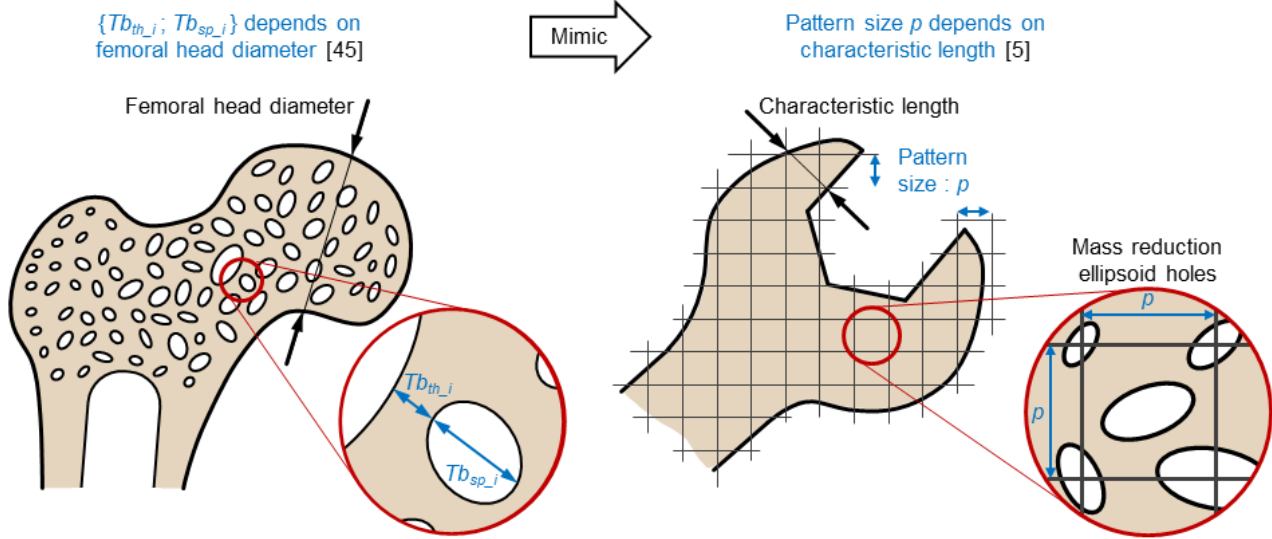
##### 3.1.1 Method bio-inspired from the trabecular bone structure

Through bone turnover, the trabecular bone is able to form and resorb bone material depending on the mechanical stresses. The following method will focus on the resorption mechanism (material removing).

In the bone, the 3D geometry has an anisotropic mechanical behavior. It can be represented in mechanics by an ellipsoidal fabric tensor [42] [43] oriented along the principal mechanical stresses. Trabecular bone contains thin bone material walls separated by porosities. The thickness of these walls is named the trabecular thickness,  $Tb_{th}$  [44]. The distance between two trabecula is named the trabecular separation,  $Tb_{sp}$  [44] (Fig. 3a). A mathematical link has been found between the femoral head diameter and the values of  $Tb_{th}$  and  $Tb_{sp}$  in multiple species [45]. Mimicking this mathematical link, Audibert et al. [5] proposed to determine a parameter "pattern size  $p$ " using the characteristic length of the studied part. This pattern size  $p$  is set to discretize the part in local areas (Fig. 3b).

(a) Femoral head

(b) Bio-inspired discretization of a ring spanner



200

**Fig. 3.** Schema of the bio-inspired discretization: (a) schema of the natural structure of the femoral head, (b) example of the discretization that could be used on a ring-spanner

205

In order to preserve the anisotropic mechanical behavior of the bone, it is decided that in the mass reduction method, the mass reduction holes will be extruded ellipses also aligned along the principal stresses. Finally, the remaining material of the part is oriented along the principal stresses. For this aim, the pattern used in the method consists in independent elliptic holes regularly arranged in a Face Centered Cubic (FCC) element of side "pattern size"  $p$ . As shown in Fig. 4, one ellipse is located at the center node of the element and one ellipse is located on each corner node of the element. These ellipses are characterized by their orientation and two main parameters: the semi-major and the semi-minor axes of the ellipse respectively noted  $a$ , and  $b$  (Fig. 4).

210

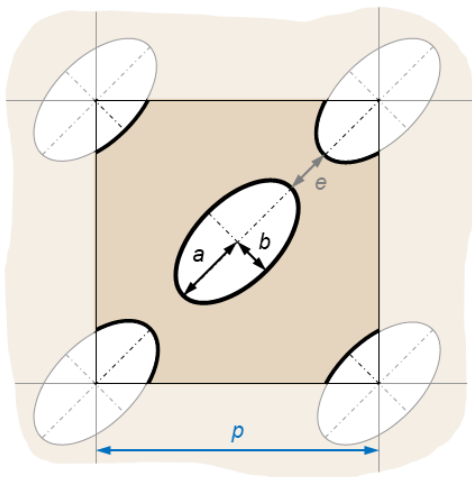


**Fig. 4.** Face Centered Cubic pattern element used in the method

215

For the next steps, the mechanical local stress distribution, in the initial part under the nominal loading, has to be known. Usually, Finite Element Analysis (FEA) is used to determine this stress distribution. This distribution will be employed to calculate the orientation and the size of the elliptic holes within the pattern. At each point of the pattern, each independent ellipse will be oriented along the major local principal stress axis. To determine the size of each ellipse ( $a$ , and  $b$ ), two steps must be carried out:

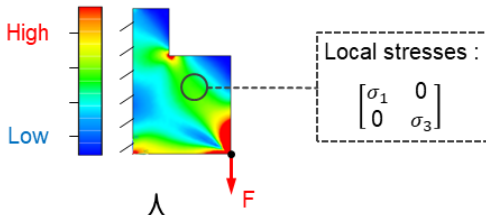
220

- *Audibert et al.* highlight a link between the local bone volume fraction  $v_f$  and local Von Mises stress  $\sigma_{VM}$  divided by its yield strength  $Re$ , resulting in nondimensionalization. This relation is given by Eq. 1 and illustrated in Fig.5a. In this relation, it can be noticed that as soon as the ratio  $\sigma_{VM}/Re$  is higher than 0.15, a volume fraction  $v_f$  equal to 1 is observed. At this value, the bone material is cortical bone.

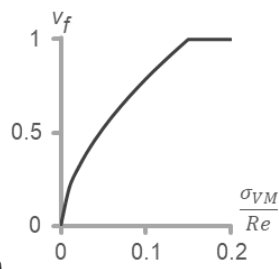
- The ratio of the semi-major and semi-minor axes of the ellipses,  $FA$ , is determined using a bio-inspired link. Indeed, [42] [43] have determined that in trabecular bone, a relation exists between the anisotropy degree of the fabric tensor and the ratio of principal stresses. Thus, in the method,  $FA$  is a function of the ratio between the major principal stress  $\sigma_1$  and the minor principal stress  $\sigma_3$ . This law is expressed in Eq. 2 [5] and based on [46] (Fig. 5b).

225

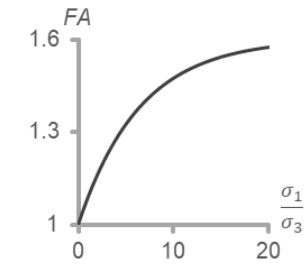
(a) Mechanical stresses in the initial part



(b)  $v_f$  as a function of  $\frac{\sigma_{VM}}{Re}$



(c)  $FA$  as a function of  $\frac{\sigma_1}{\sigma_3}$



(d) Material cohesion diagram

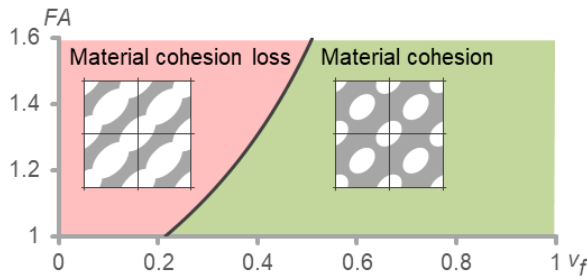


**Fig. 5.** Relations between the parameters used in the method: (a) Volume fraction  $v_f$  as a function of the ratio of Von Mises stresses  $\sigma_{VM}$  over the yield strength  $Re$ , (b) Ratio  $FA$  as a function of the ratio of principal stress  $\sigma_1$  over principal stress  $\sigma_3$ , (c)  $FA$  as a function of  $v_f$ , representing the domains where material cohesion is lost (red) or is maintained (green)

230

$$v_f = 3.07 * \left(\frac{\sigma_{VM}}{Re}\right)^{0.59} \quad (1)$$

$$FA = \frac{a}{b} = 1.6 - 0.6 \exp\left(\frac{-1}{6.45} \left|\frac{\sigma_1}{\sigma_3}\right|\right) \quad (2)$$

Finally, knowing the pattern size  $p$ , the volume fraction  $v_f$  and the ratio  $FA$ , the dimensions of the semi axes of the ellipse  $a$  and  $b$  can be determined.

235

### 3.1.2 Material cohesion-loss identification

However, this method entails a mass reduction limit due to the 2.5D approach and to the pattern shape. Indeed, if the ellipses are too large, two nearby ellipses will intersect. The resulting hole might alter dramatically the local mechanical performances of the structure. If this phenomenon occurs in a large area of the mechanical part, material cohesion is compromised. Fig. 5c illustrates the relation between this matter cohesion/cohesion-loss inside a 2.5D part and the couple  $\{v_f; FA\}$ . The calculations have been done in the "worst case", where the ellipses are oriented in the diagonal axis of the pattern. Indeed, the ellipses

240

intersect the fastest in this configuration for a given couple  $\{v_f; FA\}$ . It ensures that for a given couple, the pattern remains conservative: material cohesion is maintained if the ellipses of the pattern have different orientations.

In Fig. 5c, the abscissa axis represents the local volume fraction,  $v_f$ , that goes from 0 (no material, only void) to 1 (no void, only material) in the local area. The figure ordinate axis represents the ratio  $FA$  of ellipses that goes from 1 ( $a=b$ ) to the limit of 1.6 ( $a=1.6*b$ ). In Fig. 5c, the red domain represents all the couples  $\{v_f; FA\}$  that cause material cohesion-loss and the green domain represents all the couples  $\{v_f; FA\}$  that maintain material cohesion. The equation of the frontier between the two domains will be presented in Section 3.2. On Fig. 5c, to ensure the material cohesion (green domain) at any point of the part (for any  $\{v_f; FA\}$  couple), the local volume fraction  $v_f$  has to be higher than 0.55. For this reason, Audibert *et al.* define a minimal threshold for the local volume fraction set to  $v_f=0.55$ . Whereas the Audibert's method has to avoid material cohesion-loss, the BIMRIM will use thresholds in order to identify the part areas where material cohesion-loss may appear. These areas correspond to barely loaded zones that Nature would probably have removed. Section 3.2 will present the iterative process of mass reduction using a variation of this threshold.

To summarize, these two last sub-sections presented a mass reduction method based on trabecular bone structure. In this method, a material cohesion-loss phenomenon appeared. The frontier between the material cohesion domain and the domain where this property is lost will be studied in the next sub-section.

### 3.1.3 Material cohesion domain definition

To define the volume fraction thresholds, the frontier seen in Fig. 5c from material cohesion domain (green domain) to the other (red domain) will be first studied. In the method presented in Section 3.1.1, the ellipses of the pattern are independent and their sizes and orientations depend on the local mechanical stress field in the considered pattern point. This independency brings an infinite number of possibilities in terms of mass reduction pattern. To be conservative, the equation of the frontier (Fig. 5c) will be calculated with equal ellipses aligned in the diagonal axis of the FCC element (Fig. 3). In this case, the material volume fraction is defined in Eq. 3 with  $e$  the distance between two ellipses (Eq. 4).

$$v_f p^2 = p^2 - 2\pi ab \quad (3)$$

$$e = \frac{\sqrt{2}}{2}p - 2a \quad (4)$$

The frontier between each material cohesion domain is defined when two ellipses are on the verge of intersecting, creating material cohesion-loss. Therefore, the space between two ellipses is set as  $e=0$  (Eq. 5).

$$a = \frac{\sqrt{2}}{4}p \quad (5)$$

Mixing Eq. 2, Eq. 3 and Eq. 5, the direct link between the volume fraction  $v_f$  and the shape factor  $FA$  is obtained (Eq. 6). This equation is plotted in Fig. 5c (blue line on the plot).

$$v_f = 1 - \frac{\pi}{4 FA} \quad (6)$$

## 3.2 Mass reduction method mimicking medullar cavity controlling material cohesion-loss

In BIMRIM, using the previous material cohesion domain, the material cohesion-loss is avoided and mass reduction is improved.

### 3.2.1. Iterative process

BIMRIM is bio-inspired by the iterations that generate the medullar cavity in long bones. In this method, unlike Nature that is able to form and resorb bone material, material will be only removed to reduce the mass of the mechanical part. The general algorithm of BIMRIM is presented in Fig 6. In the first part of the BIMRIM algorithm named cavity design process, removable material is successively identified using Mass Removing Thresholds (MRT) (Section 3.2.2). At each iteration, material areas are removed from the part, so the mechanical stresses are redistributed in the remaining material given that the boundary conditions remain constant. In order to keep removing material during the whole process, the MRT evolves as presented in Section 3.2.2. In the second part of BIMRIM algorithm, the method presented in section 3.1.1 is used with a minimal volume fraction set at 0.55 in order to avoid material cohesion-loss. This last iteration generates independent separated elliptic holes.

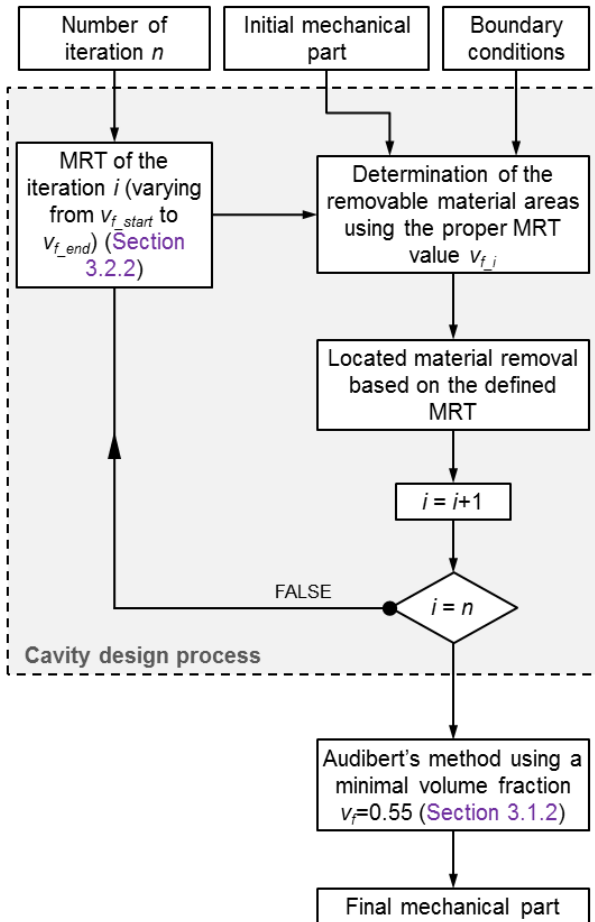


Fig. 6. Bio-inspired algorithm

### 3.2.2 Definition of Mass Removing Thresholds

In the cavity design process (Fig. 6) of BIMRIM, a MRT represents the limit where the material is considered removable or not. This threshold is based on the mechanical stresses that an area undergoes. If the local volume fraction is below the MRT (corresponding to low mechanical stresses), the material can be removed. At each iteration, the definition of this threshold is based on the material cohesion/cohesion-loss domains.

Two extrema MRTs are defined in terms of volume fraction thresholds that are directly derived from Von Mises stresses (Eq. 1). These two extrema MRT are set as  $v_{f\_start}$  and  $v_{f\_end}$ . For each iteration, the MRT values are linearly interpolated between these two values using  $n$  iterations of material removing.

The two extrema MRT values used in the cavity design process are defined as follow:

- The starting MRT is set as  $v_{f\_start}=0.215$  for the first iteration. With the pattern defined in Fig. 3, if the local volume fraction is lower than this value, material cohesion-loss will necessarily be reached for

any ratio  $FA$  (Fig. 5c). This MRT value corresponds to circular shape of ellipses (ratio  $FA=1$ ) as shown in Fig. 7 (green schema).

- The ending MRT is set as  $v_{f\_end}=0.424$  for the last iteration. With the pattern defined in Fig. 3, if the local volume fraction is lower than this value, material cohesion-loss will appear on average. The cohesion-loss will depend on the ratio  $FA$  and the ellipse orientation (Fig. 5c). This MRT value corresponds to ellipses with average ellipsoid shape (ratio  $FA=1.36$ ) as shown in Fig. 7 (pink schema).

Between these two MRTs,  $n$  iterations will be done with a linear variation of  $v_{f\_i}$  from  $v_{f\_start}$  to  $v_{f\_end}$  with a constant step. At each iteration  $i$  with  $i \in \llbracket 1, n \rrbracket$ , the material areas that have a volume fraction lower than  $v_{f\_i}$  (Eq. 7) are removed.

$$v_{f\_i} = 0.215 + i \frac{0.424 - 0.215}{n + 1} \quad (7)$$

The complete process is illustrated in Fig. 7. For each iteration, a mechanical part  $p_i$  has its volume reduced during the mass reduction iteration using the threshold  $v_{f\_i}$  and becomes the new part  $p_{i+1}$ .

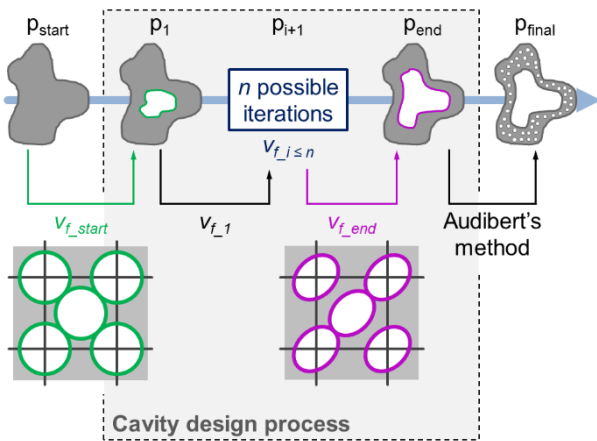


Fig. 7. BIMRIM process using the different MRT values leading to material removal

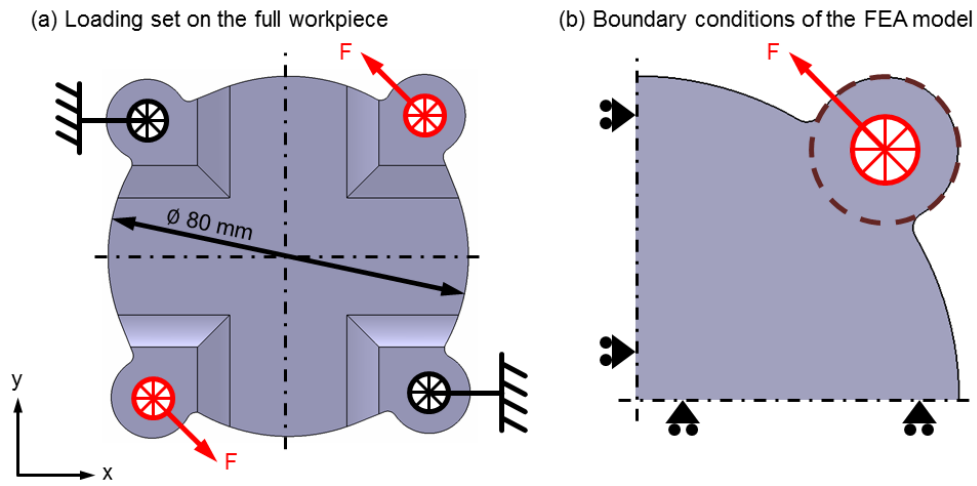
## 4 Experimental validation

### 4.1 Study case

Fig. 8 presents the sample geometry. This sample consists in a torsion disc with four lugs distributed at  $90^\circ$  from one another. Fig. 8a illustrates the full loading case applied on the initial part. This sample undergoes a torque that is simulated by two forces applied on two opposed lugs.

This study case presents a double symmetry (black dotted line on Fig. 8a) in terms of geometry and loading. Thanks to these properties, the computation focuses only on a quarter of the whole disc using sliding contacts on the symmetry planes (Fig. 8b). A node centered in the hole has a rigid connection with all the elements of the inner edge of the hole. A FEA is carried out on this quarter disc using a 2D-shell study.

Saint-Venant principle states that the stress field is incorrectly estimated close to the application points of the forces. To respect this principle, a non-removable area is defined for the cavity design process. This area is represented by a dark red dotted line in Fig. 8b. This restriction is inhibited for the iteration after the cavity design process of BIMRIM (Fig. 6 bottom section). This iteration corresponds to the use of the Audibert's method that generates small elliptical holes in the part.



335 Fig. 8. Boundary conditions applied on: (a) the full disc and (b) the simplified quarter disc

#### 4.2 BIMRIM applied on study case

BIMRIM is applied on this study case. In this experimental validation, the iteration number  $n$  (Section 3.2.2) is set to five, which provides a total of eight iterations ( $i=1$ : starting iteration,  $i=2$  to  $6$ : 5 iterations,  $i=7$ : ending iteration,  $i=8$ : Audibert's method [5]).

340 This whole process has been computed and the result of each iteration is shown in Fig. 9. For each step of BIMRIM, the MRT values are calculated using Eq. 7. The initial part  $p_{start}$  is modified by the cavity design process to obtain the  $p_{redesign}$ . To finish BIMRIM, the Audibert's method is applied on  $p_{redesign}$  to generate small elliptic holes so as to obtain the final part  $p_{final}$ . To take into account the manufacturability of the part  $p_{final}$  a minimal value of the semi-major axis is set to 0.5.

345 For each iteration, BIMRIM generates a set of elliptic holes on the whole part  $p_i$ . In Fig. 9, to simplify the viewing, only ellipses that have a volume fraction lower than the MRT value are displayed (ellipses that may intersect at this threshold). The envelop line of these ellipses is depicted by a red line. This line represents the material that is removed at each iteration.

350 Fig. 9 highlights that at each iteration of the cavity design process, material is removed from the inner part of the disc. In addition, from iteration 5 to the end of the cavity design process (iteration 7), material is also removed from the external part of the disc. These two phenomena generate the square frame shape of  $p_{redesign}$ .

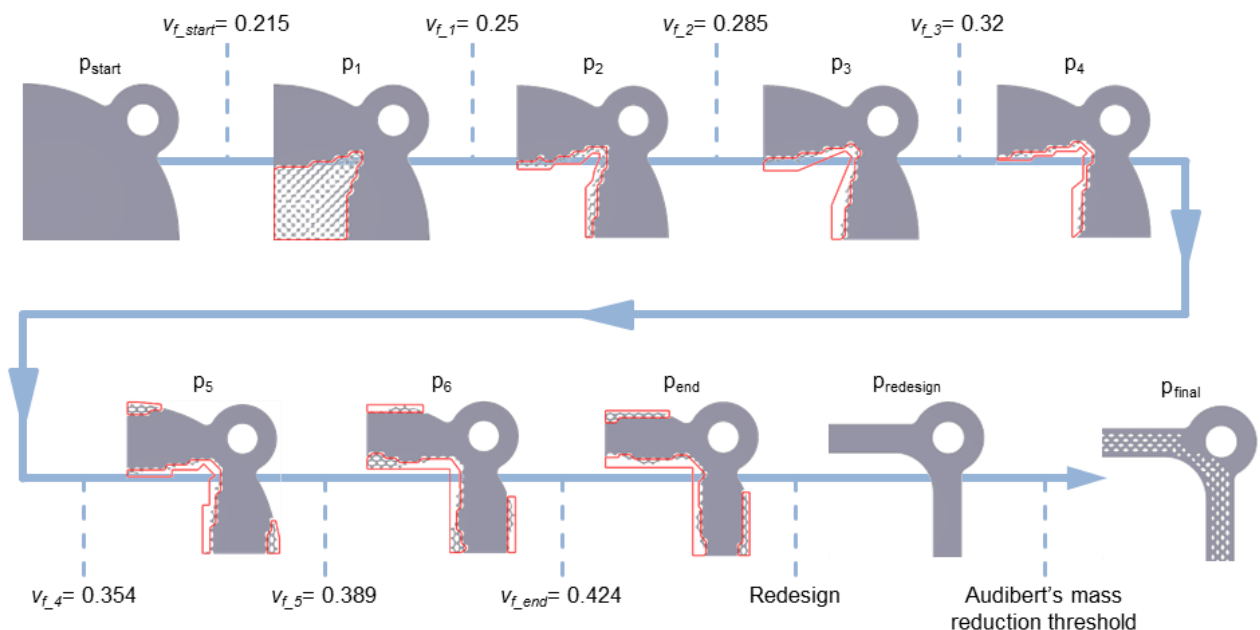


Fig. 9. BIMRIM process applied on the torsion disc

Fig. 10 presents the two main stages of BIMRIM: results of the cavity design process  $p_{\text{redesign}}$  and the final bio-inspired part  $p_{\text{final}}$ . In this study case, BIMRIM reduced the mass of the part by 60.3%.

In this study, TO is used as a standard to evaluate the performances of BIMRIM. The mass of the bio-inspired final part is taken as the target mass for the TO method. No geometrical constraints are imposed on this method. The redesign step of the process induces a small mass deviation between the two final geometries (less than 4%).

Fig. 10 highlights the fact that the square shape is common for both final geometries (BIMRIM and TO). The main difference between the two designs is the width of branches that is slightly bigger for the part obtained through BIMRIM. This width increase in BIMRIM part is permitted because of the additional mass reduction induced by the small elliptic holes.

365

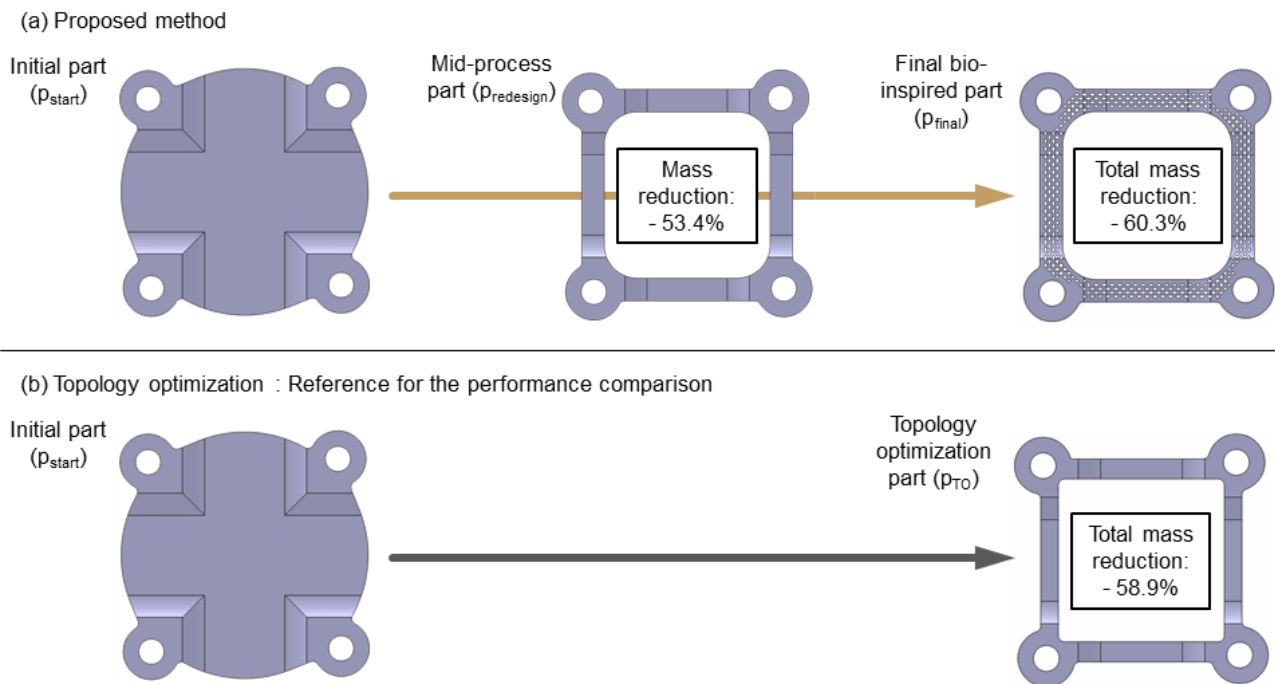


Fig. 10. (a) Main stages in the BIMRIM process on the torsion disc with the initial part, the mid-process part obtained with the cavity design process, the final part obtained with the BIMRIM, compared to the TO process (b)

### 4.3 Experiment device

The bench test device (Fig. 11) is designed to evaluate the torsional stiffness of both parts:  $p_{\text{final}}$  and  $p_{\text{TO}}$ . On this device, two lugs of the part are fixed on a multicomponent dynamometer (fixed on the device frame), and the two others are attached to a torsion lever. A displacement is applied on the lever to generate a rotation on the two lugs attached to the lever that will deform the workpiece. This deformation generates a torque which is measured by the dynamometer.

The two parts are 3D-printed with polymer material. The masses of the two printed workpieces are nearly equal (Fig. 12 top section).

375

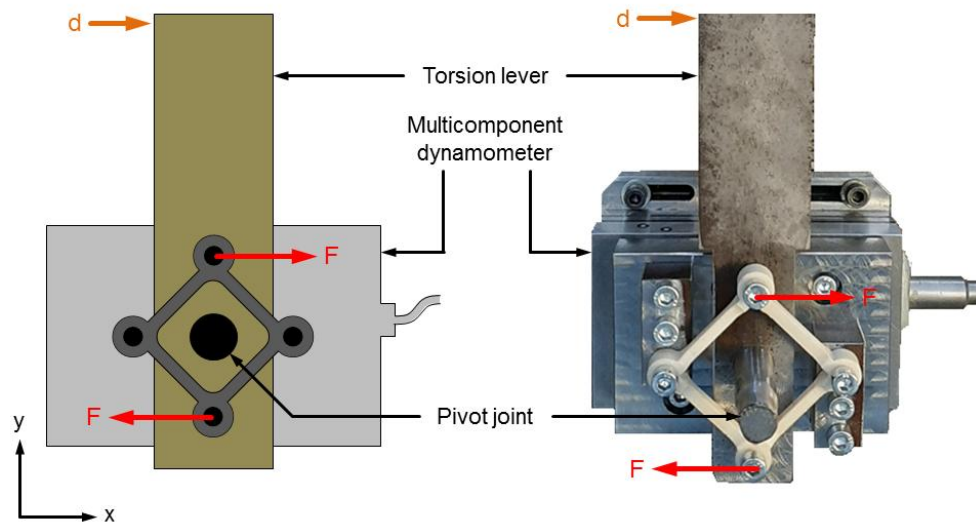


**Fig. 11.** Schema of the bench test designed to carry out the experimental validation of both BIMRIM and TO parts (left section) and the used test bench (right section)

#### 4.4 Experimental test results

**Fig. 12** presents a picture of each printed part with their mass value and the chart of their torsional stiffness. This chart plots the measured torque as a function of the angular displacement applied on the torsion lever, for both sample. A third degree polynomial was best fitted, using least squares method, to the measured data ( $f_1$  for BIMRIM and  $f_2$  for TO).

It can be observed that both curves present a progressive increase of their slope during the test. This chart shows that the stiffness of the bio-inspired part,  $p_{final}$ , is substantially higher than that of the TO,  $p_{TO}$ . The comparison of the two polynomials ( $f_1$  and  $f_2$ ) highlights the fact that regarding their torsional stiffness, the BIMRIM part is 27% stiffer than the TO part.

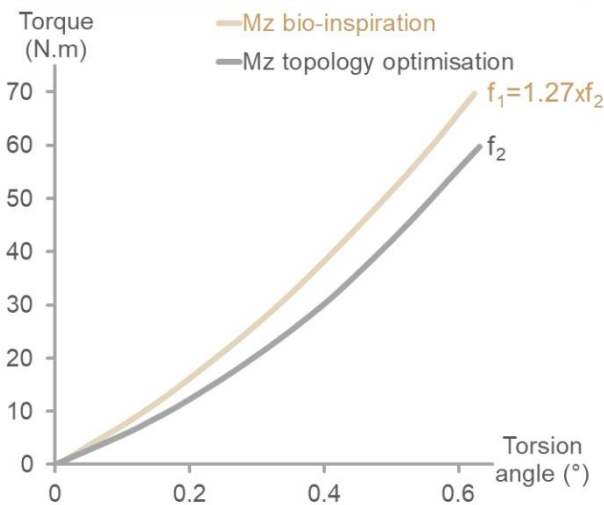
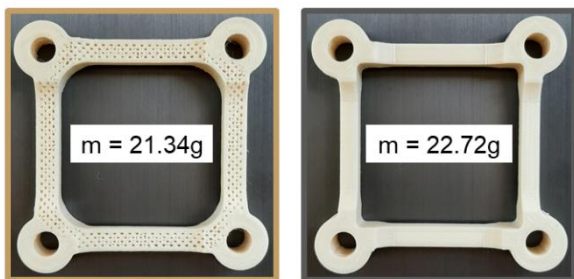


**Fig. 12.** Printed parts and their respective mass (BIMRIM in the top left section and TO in top right section), and the obtained curves relating the torque as a function of the torsion angle for both BIMRIM and TO parts (in the bottom section)

## 4.5 Discussion

In Section 4.4, the results of experiments highlighted the fact that the BIMRIM part is 27% stiffer than the TO part. The current sub-section investigates on the origin of this gain.

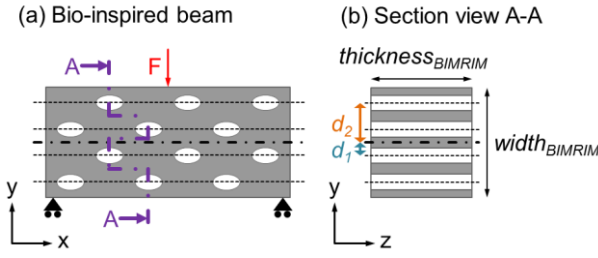


**Fig. 13.** Schema of the branches of the BIMRIM part (a) and the section view A-A which is used to determine the BIMRIM part's quadratic moment of area (b)

The parts can be considered as four perpendicular beams linked by lugs off-centered from the neutral fiber of the beam. It can be assumed that each beam undergoes multiples loadings:

- Traction and compression with a risk of having buckling added to the compression
- Bending due to the off-set between the lugs' centers and the beams' axes

In both instances, the corresponding quantities are linked to the beam quadratic moment of area. Indeed, both beams differ only in their width. These quadratic moments of area are calculated as follows:

- The TO part's quadratic moment of area,  $I_{TO}$ , is calculated from the general formula (Eq. 8). This equation depends on the thickness of the TO beam ( $thickness_{TO}$ ) and the width of the TO beam ( $width_{TO}$ ). The numerical application leads to  $I_{TO}=1.08 \times 10^{-10} \text{ m}^4$ .
- The BIMRIM part's quadratic moment of area,  $I_{BIMRIM}$ , is calculated along the section with parallel planes in the worst case: all the ellipses are located along the same x-abcissa (Fig. 13b). These planes are orthogonal to the general direction of the beam (purple dotted line in Fig. 13a).  $I_{BIMRIM}$  is composed of the quadratic moment of area of: first, the filled beam (which depends on the beam's thickness ( $thickness_{BIMRIM}$ ) and on the beam's width ( $width_{BIMRIM}$ )) and second, the porosities transferred on the neutral axis of the beam (Eq. 9) calculated using the parallel axis theorem of Huygens (Eq. 10). In this calculation, the porosities are considered uniform. In addition, since the ellipses are two by two equidistant from the beam neutral axis with distances  $d_1$  and  $d_2$ , simplifications of the equations can be done. Finally, with these considerations, the final formula is calculated (Eq. 11). The numerical application leads to  $I_{BIMRIM}=1.405 \times 10^{-10} \text{ m}^4$ .

The ratio between these two quadratic moments of area shows that  $I_{BIMRIM}$  is 30% higher than  $I_{TO}$ . This theoretical comparison reinforces the view that the section of the beams is the origin of the part stiffness.

$$I_{TO} = \frac{thickness_{TO} * width_{TO}^3}{12} \quad (8)$$

$$I_{BIMRIM} = \frac{thickness_{BIMRIM} * width_{BIMRIM}^3}{12} - \sum I_{porosity}' \quad (9)$$

$$I_{porosity}' = I_{porosity} + S_{porosity} * d^2 \quad (10)$$

$$I_{BIMRIM} = \frac{thickness_{BIMRIM} * width_{BIMRIM}^3}{12} - 4 * I_{porosity} - 2 * S_{porosity} * (d_1^2 + d_2^2) \quad (11)$$

## 420 5 Conclusions

This paper presents a 2.5D method, bio-inspired from long bone internal structure, to significantly reduce mass of mechanical parts. In the literature, a method bio-inspired from trabecular bone structure was defined to reduce the mass of parts. This stress-driven method adds porosities bio-inspired in three ways: bio-inspired in shape (elliptic holes), bio-inspired in orientation (along the principal stress axes) and bio-  
425 inspired in size. But this method presents material cohesion-loss limitation. Improving on this method and including cavity design process, a new approach was defined in this paper to reach more significant mass reduction on mechanical parts. This BIMRIM (Bio-Inspired Mass Reduction Iterative Method) is based on long bone medullar cavity structure. The benefits of BIMRIM are as follows:

- It uses iteratively the method bio-inspired from trabecular bone structure in order to identify barely  
430 loaded areas of the mechanical part that are removed. This successive removal of material allows for a redistribution of the predicted mechanical stresses in the part. This process determines more accurately the stress field in the remaining material.
- The cavity design process identifies and suppresses large unloaded areas. At the end of the algorithm, the method bio-inspired from trabecular bone is applied to finalize the mass reduction  
435 process. The generated geometry is similar to long bone, combining trabecular bone areas and medullar cavity areas.
- A physical experimental test is carried out on a torsion disc. In this test, the method leads to a 60% mass reduction from the initial disc. TO method was computed with the same mass objective and was used as a standard to compare the torsional stiffness of BIMRIM part. As a result of the  
440 experiments, the BIMRIM part presented a 27% higher torsional stiffness, at equal mass, than the TO part.

The proposed method provides convincing results in 2.5D that opens the way to promising results in 3D.

### CRedit authorship contribution statement

- 445 Mathieu Bilhère-Dieuzeide: Conceptualization, Data curation, Formal analysis, Investigation, Methodology, Resources, Software, Visualization, Writing - original draft, Writing - review & editing
- Julien Chaves-Jacob: Conceptualization, Formal analysis, Funding acquisition, Investigation, Methodology, Project administration, Resources, Software, Supervision, Validation, Visualization, Writing - original draft, Writing - review & editing
- 450 Jean-Marc Linares: Conceptualization, Formal analysis, Funding acquisition, Investigation, Methodology, Project administration, Supervision, Validation, Visualization, Writing - review & editing
- Emmanuel Buhon: Conceptualization, Formal analysis, Funding acquisition, Investigation, Methodology, Project administration, Resources, Software, Supervision, Validation, Writing - review & editing
- 455 Guillaume Biguet-Mermet: Conceptualization, Formal analysis, Funding acquisition, Investigation, Methodology, Project administration, Resources, Software, Supervision, Validation, Writing - review & editing

### Declaration of Competing Interest

- 460 The authors declare that they have no known competing financial interests or personal relationships that could have appeared to influence the work reported in this paper.

### Aknowledgment

- 465 The experimental equipment was funded by the European Community, French Ministry of Research and Education and Aix-Marseille Conurbation Community. Authors aknowledge the Association Nationale Recherche Technologie (France) for financial support through a Convention Industrielle de Formation par la Recherche fund (Cifre thesis n°2020/0881).

## References

- 470 [1] M.K. Thompson, G. Moroni, T. Vaneker, G. Fadel, R.I. Campbell, I. Gibson, A. Bernard, J. Schulz, P. Graf, B. Ahuja, Design for additive manufacturing: trends, opportunities, considerations, and constraints, *CIRP Annals* 65 (2016) 737-760, <https://doi.org/10.1016/j.cirp.2016.05.004>
- [2] Y. Ding, Shape optimization of structures : a literature survey, *Computers and Structures* Vol. 24 N°6 (1986) 985-1004, [https://doi.org/10.1016/0045-7949\(86\)90307-X](https://doi.org/10.1016/0045-7949(86)90307-X)
- 475 [3] G. Allaire, F. Jouve, A.M. Toader, Structural optimization using sensitivity analysis and a level-set method, *Journal of Computational Physics* 194: 1 (2004) 363-393, <https://doi.org/10.1016/j.jcp.2003.09.032>
- [4] Q. Xia, T. Shi, S. Liu, M.Y. Wang, A level set solution to the stress based structural shape and topology optimization, *Computers and Structures* 90-91 (2012) 55-64, <https://doi.org/10.1016/j.compstruc.2011.10.009>
- 480 [5] C. Audibert, J. Chaves-Jacob, J.M. Linares, Q.A. Lopez, Bio-inspired method based on bone architecture to optimize the structure of mechanical workpieces, *Materials & Design* 160 (2018) 708-717, <https://doi.org/10.1016/j.matdes.2018.10.013>
- [6] Q. Xia, M.Y. Wang, Topology optimization of thermoelastic structures using level set method, *Comput. Mech.* 42 (2008) 837-857, <https://doi.org/10.1007/s00466-008-0287-x>
- 485 [7] P.D. Dunning, C.J. Brampton, H.A. Kim, Simultaneous optimization of structural topology and material grading using level set method, *Materials Science and Technology* 31: 8 (2015) 884-894, <https://doi.org/10.1179/1743284715Y.0000000022>
- [8] G. Dong, Y. Tang, Y. F. Zhao, A survey of modelling of lattice structures fabricated by additive manufacturing, *Journal of Mechanical Design* 139: 10 (2017), <https://doi.org/10.1115/1.4037305>
- 490 [9] Scerrato, A.M. Bersani, I. Giorgio, Bio-inspired design of a porous resorbable scaffold for bone reconstruction: a preliminary study, *Biomimetics* 6: 18 (2021), <https://doi.org/10.3390/biomimetics6010018>
- [10] Z. Xiao, Y. Yang, R. Xiao, Y. Bai, C. Song, D. Wang, Evaluation of topology-optimized lattice structures manufactured via selective laser melting, *Materials & Designs* 143 (2018) 27-37, <https://doi.org/10.1016/j.matdes.2018.01.023>
- 495 [11] O. Al-Ketan, R. Rowshan, R.K. Al-Rub, Topology-mechanical property relationship of 3D printed strut, skeletal, and sheet based periodic metallic cellular materials, *Additive Manufacturing* 19 (2018) 167-183, <https://doi.org/10.1016/j.addma.2017.12.006>
- 500 [12] T. Yu, H. Hyer, Y. Sohn, Y. Bai, D. Wu, Structure-property relationship in high strength and lightweight AlSi10Mg microlattices fabricated by selective laser melting, *Materials & Design* 182: 108062 (2019), <https://doi.org/10.1016/j.matdes.2019.108062>
- [13] A. Panesar, M. Abdi, D. Hickman, I. Ashcroft, Strategies for functionally graded lattice structures derived using topology optimization for additive manufacturing, *Additive Manufacturing* 19 (2018) 81-94, <https://doi.org/10.1016/j.addma.2017.11.008>
- 505 [14] A. Seharing, A.H. Azman, S. Abdullah, A review on integration of lightweight gradient lattice structures in additive manufacturing parts, *Advances in Mechanical Engineering* 12: 6 (2020) 1-21, <https://doi.org/10.1177/1687814020916951>
- [15] S. Maietta, A. Gloria, G. Improta, M. Richetta, R. de Santis, M. Matorelli, A further analysis on Ti6Al4V lattice structures manufactured by selective laser melting, *Journal of Healthcare Engineering* (2019), <https://doi.org/10.1155/2019/3212594>
- 510 [16] X. Wang, L. Zhu, L. Sun, N. Li, Optimization of graded filleted lattice structures subject to yield and buckling constraints, *Materials & Design* 206: 109746 (2021), <https://doi.org/10.1016/j.matdes.2021.109746>
- 515 [17] C. Pan, Y. Han, J. Lu, Design and optimization of lattice structures: a review, *Applied Sciences* 10: 18 (2020), <https://doi.org/10.3390/app10186374>
- [18] D.W. Abueidda, M. Elhebeary, C.S. Shiang, S. Pang, R.K. Al-Rub, I.M. Jasiuk, Mechanical properties of 3D printed polymeric gyroid cellular structures: experimental and finite element study, *Materials & Design* 165: 107597 (2019), <https://doi.org/10.1016/j.matdes.2019.107597>

- 520 [19] J. Shi, L. Zhu, L. Li, Z. Li, J. Yang, X. Wang, A TPMS-based method for modeling porous scaffolds  
for bionic bone tissue engineering, *Scientific Reports* 8 (nature.com) 2018,  
<https://doi.org/10.1038/s41598-018-25750-9>
- [20] D. Kang, S. Park, Y. Son, S. Yeon, S.H. Kim, I. Kim, Multi-lattice inner structures for high-strength  
and light-weight in metal selective laser melting process, *Materials & Design* 175: 107786 (2019),  
525 <https://doi.org/10.1016/j.matdes.2019.107786>
- [21] X. Jin, G.X. Li, M. Zhang, Optimal design of three-dimensional non-uniform nylon lattice structures  
for selective laser sintering manufacturing, *Advances in Mechanical Engineering* 10: 7 (2018),  
<https://doi.org/10.1177/1687814018790833>
- [22] D. Li, W. Liao, N. Dai, Y.M. Xie, Anisotropic design and optimization of conformal gradient lattice  
530 structures, *Computer-Aided Design* 119 (2020), <https://doi.org/10.1016/j.cad.2019.102787>
- [23] D. Li, N. Dai, Y. Tang, G. Dong, Y.F. Zhao, Design and optimization of graded cellular structures  
with triply periodic level surface-based topological shapes, *Journal of Mechanical Design* 141: 7 (2020),  
<https://doi.org/10.1115/1.4042617>
- [24] A. Ghazlan, T. Nguyen, T. Ngo, S. Linforth, V.T. Le, Performance of a 3D printed cellular structure  
535 inspired by bone, *Thin-Walled Structures* 151 (2020), <https://doi.org/10.1016/j.tws.2020.106713>
- [25] M.C. Fernandes, J. Aizenberg, J.C. Weaver, K. Bertoldi, Mechanically robust lattices inspired by  
deep-sea glass sponges, *Nature Materials* 20 (2021) 237-241, <https://doi.org/10.1038/s41563-020-0798-1>
- [26] A. du Plessis, C. Broeckhoven, I. Yadroitsava, C.H. Hands, R. Kunju, D. Bhate, Beautiful and  
540 Functional: A Review of Biomimetic Design in Additive Manufacturing, *Additive manufacturing* 27 (2019)  
408-427, <https://doi.org/10.1016/j.addma.2019.03.033>
- [27] Z. Wang, N. Wu, Q. Wang, Y. Li, Q. Yang, F. Wu, Novel Bionic Design Method for Skeleton  
Structures Based on Load Path Analysis, *Applied Sciences* 10: 22 (2020),  
<https://doi.org/10.3390/app10228251>
- 545 [28] N.S. Ha, G. Lu, A review of recent research on bio-inspired structures and materials for energy  
absorption applications, *Composite Part B* 181: 107496 (2020),  
<https://doi.org/10.1016/j.compositesb.2019.107496>
- [29] S.E. Naleway, M.M. Porter, J. McKittrick, M.A. Meyers, Structural design elements in biological  
materials: application to bioinspiration, *Advanced Materials* 27 (2015) 5455-5476,  
550 <https://doi.org/10.1002/adma.201502403>
- [30] P. Fratzl, R. Weinkamer, Nature's hierarchical materials, *Progress in materials science* 52: 8  
(2007) 1263-1334, <https://doi.org/10.1016/j.pmatsci.2007.06.001>
- [31] I. Giorgio, M. Spagnuolo, U. Andreaus, D. Scerrato, A.M. Bersani, In-depth gaze at the astonishing  
mechanical behavior of bone: a review for designing bio-inspired hierarchical materials, *Mathematics*  
555 and *Mechanics of Solids* 26:7 (2020) 1074-1103, <https://doi.org/10.1177%2F1081286520978516>
- [32] M.A. Meyers, P.Y. Chen, A.Y. M. Lin, Y. Seki, Biological materials: structure and mechanical  
properties, *Progress in Materials Science* 53: 1 (2008) 1-206,  
<https://doi.org/10.1016/j.pmatsci.2007.05.002>
- 560 [33] C. Ruff, B. Holt, E. Trinkaus, Who's afraid of the big bad Wolff ? : "Wolff's law" and bone functional  
adaptation, *American Journal of Physical Anthropology* 129: 4 (2006) 484-498,  
<https://doi.org/10.1002/ajpa.20371>
- [34] J.H. Gosman, R.A. Ketcham, Pattern in ontogeny of human trabecular bone from SunWatch Village  
in the prehistoric Ohio Valley: general features of microarchitectural change (dissertation), *American*  
*Journal of Physical Anthropology* 138 (2009) 318-332, <https://doi.org/10.1002/ajpa.20931>
- 565 [35] C. Boyle, I.Y. Kim, Three-dimensional micro-level computational study of Wolff's law via trabecular  
bone remodeling in the human proximal femur using design space topology optimization, *Journal of*  
*Biomechanics* 44: 5 (2011) 935-942, <https://doi.org/10.1016/j.jbiomech.2010.11.029>
- [36] A. Nazarian, J. Muller, D. Zurakowski, R. Muller, B.D. Snyder, Densitometric, morphometric and  
mechanical distribution in the human proximal femur, *Journal of Biomechanics* 40: 11 (2007) 2573-  
570 2579, <https://doi.org/10.1016/j.jbiomech.2006.11.022>
- [37] B. Willie, G. N. Duda, R. Weinkamer, Chapter 2 : Bone structural adaptation and Wolff's law, in: P.  
Fratzl, J. W. C. Dunlop, R. Weinkamer, *Materials design inspired by nature : function through inner*  
*architecture*, RSC Smart Materials 4, 2013, pp.17-45, <https://doi.org/10.1039/9781849737555>

- 575 [38] T.M. Ryan, G.E. Krovitz, Trabecular bone ontogeny in the human proximal femur, *Journal of Human Evolution* 51: 6 (2006) 591-602, <https://doi.org/10.1016/j.jhevol.2006.06.004>
- [39] T. Lekszycki, Functional adaptation of bone as an optimal control problem, *Journal of Theoretical and Applied Mechanics* 43: 3 (2005) 555-574
- [40] I. Vuori, A. Heinonen, Chapter 19 : Sport and Bone, in: B.L. Drinkwater, *Women in Sport Volume 8 of the encyclopedia of sports medicine*, Blackwell Science, 2000, pp.280-300
- 580 [41] R. Huiskes, R. Ruimerman, G.H. van Lenthe, J.D. Janssen, Effects of mechanical forces on maintenance and adaptation of form in trabecular bone, *Nature* 405 (2000) 704-706, <https://doi.org/10.1038/35015116>
- [42] T.P. Harrigan, R.W. Mann, Characterization of Microstructural Anisotropy in Orthotropic Materials using a Second Rank Tensor, *Journal of Materials Science* 19 (1984) 761-767, <https://doi.org/10.1007/BF00540446>
- 585 [43] S.N. Musy, G. Maquer, J. Panyasantisuk, J. Wandel, P.K. Zysset, Not only stiffness, but also yield strength of the trabecular structure determined by non-linear  $\mu$ FE is best predicted by bone volume fraction and fabric tensor, *Journal of the Mechanical Behavior of Biomedical Materials* 65 (2017), 808-813, <https://doi.org/10.1016/j.jmbbm.2016.10.004>
- 590 [44] A.M. Parfitt, M.K. Drezner, F.H. Glorieux, J.A. Kanis, H. Malluche, P.J. Meunier, S.M. Ott, R.R. Recker, Bone Histomorphometry: Standardization of Nomenclature, Symbols and Units, *Journal of Bone and Mineral Research* 2: 6 (1987) 595-610, <https://doi.org/10.1002/jbmr.5650020617>
- [45] M. Doube, M.M. Kłosowski, A.M. Wiktorowicz-Conroy, J.R. Hutchinson, S.J. Shefelbin, Trabecular bone scales allometrically in mammals and birds, *Proceedings of the Royal Society B* 278: 1721 (2011) 3067-3073, <https://doi.org/10.1098/rspb.2011.0069>
- 595 [46] K.I. Tsubota, Y. Suzuki, T. Yamada, M. Hojo, A. Makinouchi, T. Adachi, Computer simulation of trabecular remodeling in human proximal femur using large-scale voxel FE models: approach to understanding Wolff's law, *Journal of biomechanics* 42: 8 (2009) 1088-1094, <https://doi.org/10.1016/j.jbiomech.2009.02.030>